Materials Today Bio 28 (2024) 101215

Contents lists available at ScienceDirect

Materials Today Bio

journal homepage: www.journals.elsevier.com/materials-today-bio

Protein corona dynamicity contributes to biological destiny disparities of nanoparticles

Liang Zhang [1], Tao Sun [1], Mingfu Gong [**,1], Chunyu Zhou, Yue Zhao, Wansu Zhang, Zhipeng Zhang, Shilin Xiao, Xiaofeng Yang, Miaomiao Wang, Xu Liu, Qian Xie, Dong Zhang [*]

Department of Radiology, Xinqiao Hospital, Army Medical University, Chongqing, 400037, China

ARTICLE INFO

Keywords:
Protein corona
Differentiated intracellular evolution
Intracellular proteostasis disruption
Metabolic alteration
PI3K/AKT-mTOR signaling pathway

ABSTRACT

Extracellular protein coronas (exPCs), which have been identified in various biofluids, are recognized for their pivotal role in mediating the interaction between nanoparticles and the cytomembrane. However, it is still unclear whether various exPCs can induce different levels of intracellular proteostasis, which is of utmost importance in preserving cellular function, and eliciting distinct intracellular biological behaviors. To investigate this, two types of exPC-coated iron oxide nanoparticles (IONPs) are prepared and used to investigate the influence of exPCs on extracellular and intracellular biological outcomes. The results demonstrate that the formation of exPCs promotes the colloidal stability of IONPs, and the discrepancies in the components of the two exPCs, including opsonin, dysopsonin, and lipoprotein, are responsible for the disparities in cellular uptake and endocytic pathways. Moreover, the differential evolution of the two exPCs during cellular internalization leads to distinct autophagy and glycolysis activities, which can be attributed to the altered depletion of angiopoietin 1 during the formation of intracellular protein coronas, which ultimately impacts the PI3K/AKT-mTOR signaling. These findings offer valuable insights into the dynamic characteristics of exPCs during cellular internalization, and their consequential implications for cellular internalization and intracellular metabolism activity, which may facilitate the comprehension of PCs on biological effects of NPs and expedite the design and application of biomedical nanoparticles.

1. Introduction

Nanoparticles (NPs), which can serve as drug carriers or active agents for disease theranostics, have exhibited remarkable potential in biomedical applications [1–4]. However, when NPs come into contact with biological fluids, proteins in surroundings rapidly bind to their surface, forming an extracellular protein corona (exPC) and altering the "chemical identity" of the NPs to a "biological identity", which then mediates interactions between the NPs and cell membranes, including ligand recognition, targeting efficiency, and cellular internalization [5–7]. The potential coating of proteins may attenuate the degradation process of NPs, mitigate cytotoxic effect, modulate in vivo half-life, alter their uptake mechanisms, and impact the inflammatory signaling pathway [8]. Previous studies have shown that the composition of exPCs, for specific NPs, is mainly determined by the specific biological environment, especially the proteins in their surroundings [9,10]. As we know, NPs will experience disparate biofluids, which contain different protein environments, before contacting with cells in clinical practice [11,12], such as in vitro cell culture environment, blood environment, and intracellular substance, leading to the formation of various exPCs. Many reports have elucidated the influence of exPCs on NP–cytomembrane interactions, which have been demonstrated to be responsible for differences in the biological effects of cells [13,14]. However, for most therapeutic NPs, their functions are primarily performed at intracellular locations [15,16], and the discrepancy in NP–cytomembrane interaction is not enough to explain the complete differences in intracellular biological effects, as most reports have focused on the intracellular biological effect of the NPs themselves but not the PCs.

Once internalized by cells, NP-exPC complexes are transported to subcellular organelles where they exert their biological effects.

* Corresponding author.
** Corresponding author.
E-mail addresses: hummer198625@163.com (M. Gong), hszhangd@tmmu.edu.cn (D. Zhang).
[1] These authors contributed equally to this work.

https://doi.org/10.1016/j.mtbio.2024.101215
Received 15 May 2024; Received in revised form 5 August 2024; Accepted 23 August 2024
Available online 25 August 2024
2590-0064/© 2024 The Authors. Published by Elsevier Ltd. This is an open access article under the CC BY-NC license (http://creativecommons.org/licenses/by-nc/4.0/).

Nevertheless, the intracellular environment differs dramatically from the extracellular. As a result, the NP-exPC complexes may undergo exchange with native intracellular proteins, leading to the formation of new intracellular protein corona (iPC)-coated NP-iPC complexes [17, 18]. This exchange process may alter the intracellular protein composition and content by releasing extracellular proteins or adsorbing intracellular proteins, resulting in the disruption of intracellular proteostasis, which is crucial for maintaining cell physiological activities [19]. Primarily, the iPCs have been identified and used for NPs intracellular trafficking by analyzing specific proteins in subcellular organelles [20]. And recently, the iPCs-induced intracellular biological effects have also been proposed in several NPs. For example, the formation of iPCs on graphdiyne oxide nanosheet can inhibit the immunosuppressive phenotype of tumor-associated macrophages by adsorbing signal transducer and activator of transcription 3 [19]. These results propose the mechanisms of iPC-induced biological effects depend on the NPs and cells specifically. However, whether the same NPs coated with different exPCs, which are often identified during preclinical research and clinical applications, cause cells to exhibit distinct intracellular biological behaviors after internalization is unclear.

To address this issue, two types of exPCs are prepared by co-incubating iron oxide nanoparticles (IONPs) with two concentrations of serum–10 % and complete serum. These concentrations are selected due to their relevance in preclinical studies of NPs, representing the cell culture environment and the blood environment, respectively. Then the exPC-mediated cell uptake and cell biological outcomes are investigated. Proteomics analysis is conducted to identify the differences in the composition of the exPCs and their evolution during internalization by cells, which provides a possible explanation for the detected disparities in cell autophagy and glycolysis activity between the two exPCs. Our findings shed light on the dynamic evolution of PCs during the process of cell internalization and their implications for cellular internalization and downstream signaling cascades, particularly in autophagy and glycolysis. This research may contribute to a better understanding of the effects of exPCs on intracellular biological behaviors.

2. Methods and materials

2.1. Synthesis and characterization of IONPs

Citrate-capped IONPs were prepared according to our previous work [21]. Briefly, hydrophobic IONPs were synthesized through the thermal decomposition of iron pentacarbonyl in the presence of oleic acid, then the hydrophobic IONPs were transformed into hydrophilic IONPs via ligand exchange with sodium citrate at an elevated temperature. The prepared IONPs were characterized by transmission electron microscopy (TEM) (Hitachi HT-7700, Hitachi, Tokyo, Japan), X-ray diffraction (XRD) (D8 Advance, Brucker, Germany), X-ray photoelectron spectroscopy (XPS) (ESCALAB 250Xi, Waltham, MA, USA), and Fourier transform infrared (FTIR) spectroscopy (Alpha II, Bruker, Germany). The hydrodynamic radius and Zeta-potential were measured using a Nicomp ZLS Z3000 (PSS, Port Richey, FL, USA), and the Fe content was quantified using ICP−OES (CPOES7200, Thermo Fisher, USA).

2.2. Mouse serum preparation

Animal experiments were conducted according to the National Institutes of Health guidelines for the ethical use of animals in research and were approved by the Laboratory Animal Welfare and Ethics Committee of the Army Medical University. Female mice approximately 8 weeks old were used for serum preparation. Mouse whole blood was collected via cardiac puncture after anesthetization with 3 % isoflurane. The blood was left at room temperature for 2 h and centrifuged at 1500 g for 5 min, after which the resulting supernatant was collected and stored at −80 °C until use.

2.3. Preparation of lysosomal and cytoplasmic proteins from J774A.1 cells

Lysosomal proteins were prepared using a lysosomal protein extraction kit (Solarbio, Beijing, China). Briefly, approximately 1×10^7 cells were collected at 4 °C and then washed twice with phosphate buffer saline (PBS). Reagent A was added, and the solution was shaken for 10 min on ice, followed by homogenization with a Dounce homogenizer. The supernatant was then collected after centrifugation at 4000*g*. Then, centrifugation at 20,000 g for 20 min was carried out to collect the sediment, which was then resuspended in 500 μL of Reagent B. The dispersion liquid was centrifuged at 20,000 g for 20 min; then, the sediment was collected, and Reagent C (100 μL) was added to resuspend the sediment. Finally, the total lysosomal proteins were prepared by collecting the supernatant after centrifugation at 12,000 g for 20 min. The cytoplasmic proteins were extracted using a cytoplasmic protein extraction kit (Solarbio). Approximately 1×10^7 cells were washed twice with cool PBS, and then, lysis (1 mL) solution was added. The cells were subsequently collected with a cell scraper. After a 30-min lysis, the cytoplasmic proteins were obtained by collecting the supernatant after centrifugation at 12,000 g for 20 min.

2.4. IONP-PC complex preparation

Briefly, exPCs formed in the cell culture environment and blood environment were obtained by co-incubation of IONPs with 10 % and complete murine serum at 37 °C for 1 h, the mixtures were then centrifuged at 21,000 g for 25 min at 4 °C to collect the pellets. After being washed two times with PBS, the final pellets were resuspended in 100 μL of PBS for use (marked as IONP@LS and IONP@HS, respectively). The IONP@LS and IONP@HS were imaged with negative-stained TEM to confirm the coating of proteins on IONPs. Briefly, 3–5 μL sample solution was deposited onto a copper grid and allowed to sit for 5 min. Subsequently, the excess solution was removed from the periphery using filter paper. Subsequently, 5 μL was added for 0.5–1 min and then removed the excess uranium acetate with filter paper immediately. The sample was then air-dried and imaged with TEM.

To simulate the evolution of exPCs during cellular internalization [22], the two IONP-exPC complexes were incubated with lysosomal proteins at 37 °C for 1 h, and the collected pellets were resuspended in cytoplasmic proteins and further incubated at 37 °C for 1 h to prepare IONP-iPC complexes. The resulting IONP-iPC complexes were named IONP@LSC and IONP@HSC, respectively.

2.5. Preparation of gene-edited cell lines

Three different low-density lipoprotein receptor (*LDLR*)-expressing AML12 cell lines (normal, medium-low, and low *LDLR*-expressing cells) were generated via siRNA-mediated knockdown. Briefly, AML12 cells were cultured in 96-well plates and transfected with *LDLR* siRNA at concentrations of 0, 20, and 100 μM to generate normal, medium-low, and low *LDLR*-level cells, respectively. After 72 h of transfection, the *LDLR* gene expression levels were detected using quantitative reverse transcription−polymerase chain reaction (qRT-PCR) and immunofluorescence staining. An *Angiopoietin 1 (Ang 1)*-overexpressed J774A.1 cell line was generated by transfection of *Ang 1*-overexpressing plasmid. Briefly, J774A.1 cells were cultured in 96-well plates and transfected with the *Ang 1* plasmid (200 ng per well) using Lipo8000 to generate *Ang 1*-overexpressing cells. After 72 h of transfection, the Ang 1 expression level was detected using immunofluorescence staining, and the Ang 1-overexpressed cells were used for further experiments.

2.6. Cellular uptake analysis

First, the cytotoxicity of IONPs on J774A.1 cell was assessed using CCK-8 assay. Then, J774A.1, 4T1, and AML12 cells were used to test the

effect of exPCs on cellular uptake of IONPs, IONP@LS, and IONP@HS. In order to trace the internalization of NPs in J774A.1 cells by Laser Scanning Confocal Microscope (LSCM), the FITC-labeled IONPs, IONP@LS, and IONP@HS were synthesized through the EDC/NHS or co-incubation of FITC with IONPs, IONP@LS, and IONP@HS, respectively. The FITC contents around IONPs, IONP@LS, and IONP@HS were standardized to the same iron content by adjusting the amount of FITC used. The influence of FITC-labeling on the physicochemical property of IONPs, IONP@LS, and IONP@HS was analyzed by detecting the Zeta-potential before use. Subsequently, approximately 1×10^4 cells were seeded in 96-well plates and cultured overnight until cell adherence. Then, the cells were incubated with 100 μL serum-free Dulbecco's modified Eagle's medium (DMEM) containing FITC-labeled IONPs, IONP@LS, or IONP@HS (Fe = 20 μg mL^{-1}). After 2, 4, and 6 h of incubation, the cells were stained with Hoechst 33342 for 30 min and then washed with PBS three times to remove the extracellular IONPs. Then the images were obtained using a LSCM (LSM 880 Airyscan, Carl Zeiss Microscopy, Germany), and the uptake content was determined via visualization of the green fluorescence. In addition to visualize the internalization by LSCM, the TEM was also used to confirm the uptake of NPs. Briefly, the IONP@LS and IONP@HS treated J774A.1 cells were collected after 6 h co-incubation and fixed with glutaraldehyde for preparing TEM samples. Besides, the Prussian Blue staining was also used to stain the intracellular iron in AML12 cells with a Prussian Blue staining kit (Solarbio, Beijing, China). For quantitative analysis, the cells were seeded in 6-well plates and treated via a procedure similar to that described above. Finally, the cells were harvested, counted, and then digested with 0.5 mL chloroazotic to measure Fe content using ICP–OES. To further analyze the endocytosis pathway of NPs in J774A.1 cells, the cells were pre-treated with chlorpromazine, genistein, and cytochalasin D to specifically inhibit clathrin-mediated endocytosis, caveolae-mediated endocytosis, and macropinocytosis. Cells without any pre-treatments were selected as controls. After treatment with FITC-labeled IONPs, IONPs@LS, or IONPs@HS (Fe = 20 μg mL^{-1}) for 6 h, the cells were processed using a procedure similar to the workflow as mentioned above for LSCM and ICP–OES.

2.7. SDS–PAGE analysis

IONP@LS, IONP@HS, IONP@LSC, and IONP@HSC with the same Fe content were added to the protein loading buffer and then heated in a water bath at 95 °C for 5 min to fully denature the proteins. Subsequently, the samples were added to an SDS–PAGE gel and subjected to 80 V electrophoresis for 20 min and then to 120 V electrophoresis for 1 h. Coomassie blue staining was utilized to stain the gel, which was then imaged with a gel imaging system (Bio-Rad).

2.8. Label-free liquid chromatography tandem mass spectrometry (LC–MS/MS) proteomics analysis

LC–MS/MS analysis and bioinformatics analysis were conducted by PTM Biolab (Hangzhou, China). The PCs were digested into peptides with trypsin and then analyzed using Q Exactive™ HF-X mass spectrometry (Thermo Fisher Scientific). A data-dependent scanning program was used for data acquisition, and the resulting LC–MS/MS data were processed using the MaxQuant search engine (v. 1.6.15.0). The false discovery rate was set to <1 %.

2.9. RNA-seq analysis

To anatomize the effect of IONP-PCs on cell transcription, approximately 1×10^5 J774A.1 cells were seeded into 6-well plates overnight at 37 °C. Then, the cells were treated with IONPs, IONPs@LS, or IONPs@HS for 6 h at suitable concentrations (the same amount of Fe was taken up), and the untreated cells were used as negative controls. After treatment, the medium supernatant was removed, and the cells were washed 3 times with cold PBS. Then, 1 mL of TRIzol reagent was added to lyse the cells for further *RNA-seq* analysis (LC Sciences, Hangzhou, China) and gene expression verification.

2.10. Transcriptome result verification

Initially, RNAs were obtained from J774A.1 cells treated with IONPs, IONP@LS, or IONP@HS for 6 h using an RNAsimple Total RNA Kit (Tiangen, Beijing, China) and reverse-transcribed into cDNA with a PrimeScript™ 1st Strand cDNA Synthesis Kit (Takara, Dalian, China). Then, qRT–PCR was conducted with TB Green™ Premix DimerEraser™ (Takara, Dalian, China) using an ABI 7500 Real-Time PCR system (Applied Biosystems). The amplification procedure consisted of 95 °C for 2 min, followed by 40 cycles of 8 s at 95 °C and 35 s at 60 °C. The primers were synthesized by Sangon Biotech (Shanghai, China), and the sequences are listed in Table S1.

To verify the cellular uptake capacity, which acquired from Gene Set Enrichment Analysis (GSEA) analysis, the IONPs-treated cells were co-incubated with FITC-dextran and then detected with a laser scanning confocal microscope (Carl Zeiss, Oberkochen, Germany).s.

2.11. Western blot analysis

After IONP@LS and IONP@HS treatment, the cells were washed, and the total proteins were extracted and quantified by a BCA protein quantitative kit. Approximately 20 μg of proteins from each sample were analyzed by sodium dodecyl sulfate–polyacrylamide gel electrophoresis and then transferred to polyvinylidene difluoride membrane. After blocking with 3 % BSA, the membranes were incubated with primary antibodies at 4 °C overnight. HRP-conjugated goat anti-rabbit IgG antibody was used as the secondary antibody, and the bands were imaged using an Image Quant LAS 4000 (GE Healthcare Life Sciences) after staining with an Enhanced Chemiluminescent Kit (Beyotime Biotechnology, Shanghai, China).

2.12. Statistical analysis

All the data were presented as the means±SDs. Differences between the two groups were analyzed by one-tailed Student's *t*-test. Comparisons were conducted with GraphPad Prism (San Diego, CA, USA). $p < 0.05$ was considered to indicate statistical significance.

3. Results and discussion

3.1. IONPs preparation and exPCs formation

Due to their superior magnetic properties, biocompatibility, and biodegradability, IONPs had shown enormous application potential in nanotheranostics [23–25], and were selected as model NPs for subsequent experiments. IONPs were first prepared by the thermal decomposition of iron pentacarbonyl, which conferred hydrophilicity via ligand exchange and characterized comprehensively. As depicted in Fig. 1A, the prepared NPs displayed a spherical shape with good monodispersity under aqueous conditions, and the diameter was 15.8 ± 1.2 nm (Fig. S1). XRD was conducted to analyze the crystal structure of the synthesized NPs. A similar peak pattern to that of Fe_3O_4 NPs (PDF #01–1111) could be observed in Fig. 1B, confirming the successful synthesis of crystalline IONPs. The elemental composition and metal oxidation states were clarified using XPS analysis in the region of 200–800 eV (Fig. 1C). The photoelectron lines at binding energies of 712, 532, and 285 eV were identified and correspond to Fe2p, O1s, and C1s, respectively [26]. Further Dynamic Light Scattering (DLS) analysis revealed that the mean hydrodynamic diameter of the IONPs was 23.6 ± 1.1 nm in H_2O (Fig. S2), which was larger than the diameter determined via TEM and demonstrated the successful modification of the hydrophilic groups on the IONP surface.

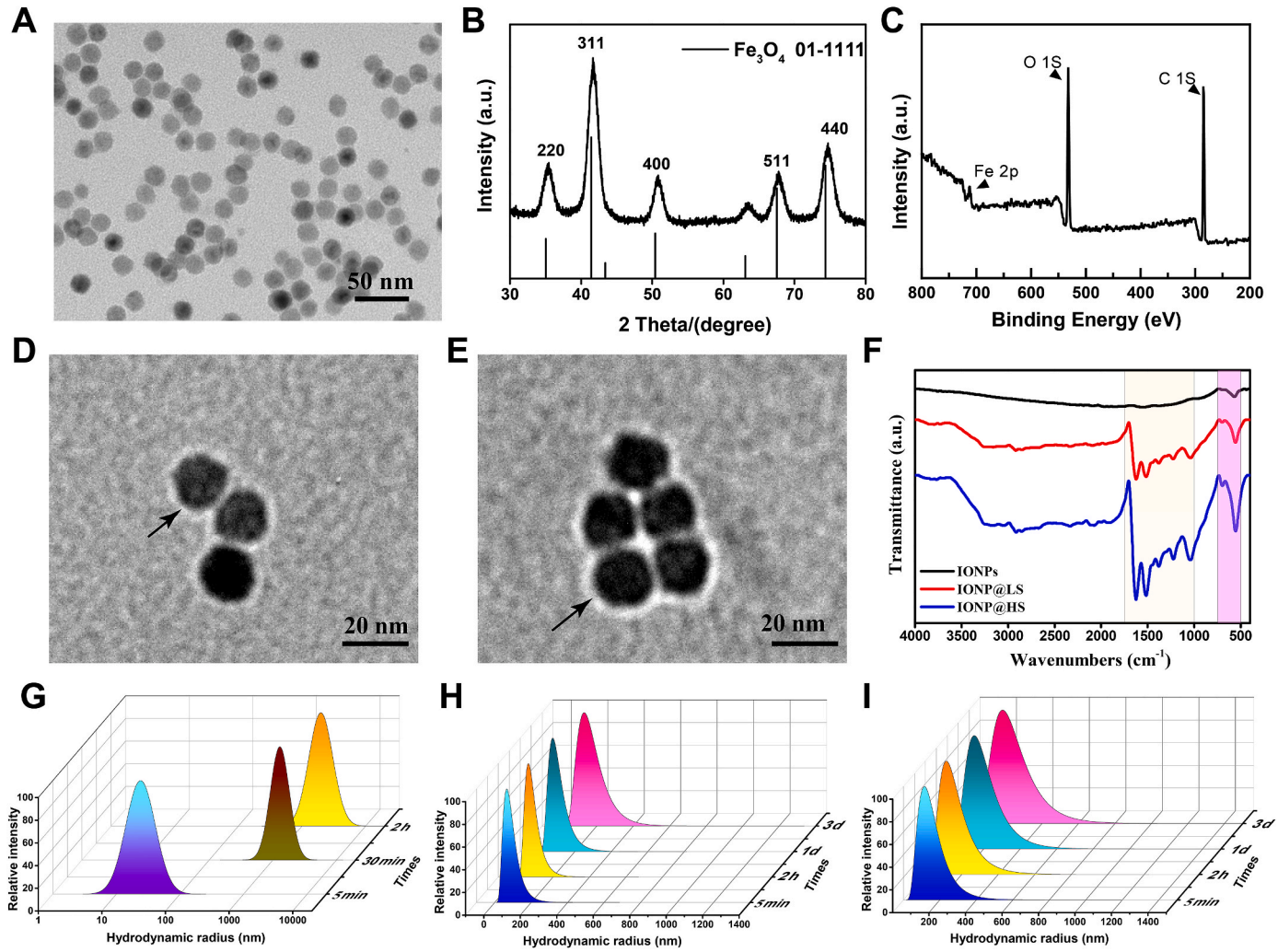

Fig. 1. IONPs characterization and exPCs formation. (A) TEM image of IONPs. (B–C) XRD pattern and XPS spectra of IONPs. (D–E) TEM images of uranyl acetate-stained IONP@LS (D) and IONP@HS (E). (F) FTIR spectra of IONPs, IONP@LS, and IONP@HS. (G–I) Hydrodynamic light scattering images showing the hydrodynamic sizes of IONPs (G), IONP@LS (H), and IONP@HS (I) in PBS at different times.

Previous studies have confirmed that intracellular biological effects of iPCs depend on the NPs and cell types specifically. However, for the same NPs with different exPCs, whether the evolution of exPCs after entering cells results in distinct metabolic regulation of the cells is still unclear. To explore this, two types of exPC-coated IONPs (denoted as IONP@LS and IONP@HS) were prepared by co-incubating IONPs with mouse serum at low and high serum concentrations, respectively. First, to explore the suitable dose of IONPs and serum used for the formation of exPCs, different concentrations (Fe = 100, 150, 200, 300, and 400 μg) of IONPs were co-incubated with 100 μL of mouse serum in a total volume of 1 mL, and then the surface exPCs were identified by SDS–PAGE. Similar protein band patterns were observed among these exPC-coated IONPs (Fig. S3), indicating that there were sufficient serum proteins (100 μL) for IONPs within the tested Fe concentrations range (100−400 μg). Hence, we incubated 200 μg of IONPs with 100 μL and 500 μL of serum in a total volume of 1 mL to prepare IONP@LS and IONP@HS, respectively. Negative-stained TEM images revealed the presence of protein layers (indicated by black arrows) surrounding the IONPs in both IONP@LS and IONP@HS groups (Fig. 1D and E), and the slight aggregation of NPs may be attributed to protein–protein interactions in the corona [27,28]. Due to the special construction of proteins (amide I), the FTIR spectrum can easily visualize the adsorbed proteins. As shown in Fig. 1F, the IONPs, IONP@LS, and IONP@HS presented similar spectrum bands of 750–500 cm^{-1}, which may be attributed to the presence of IONPs. Nevertheless, IONP@LS and IONP@HS exhibited specific spectrum bands within the range of 1750–1000 cm^{-1}, which can be attributed to the amide I vibration band [29]. To evaluate the effect of exPCs on the colloidal stability of IONPs in an environment similar to that of a physiological liquid, PBS was used to resuspend these NPs, then the hydrodynamic size was measured over an extended period. As depicted in Fig. 1G–I, although the sizes of IONP@LS and IONP@HS showed similarities in TEM images (Fig. 1D and E), a significant difference in hydrodynamic size was identified here. Upon resuspension in PBS for 5 min, the hydrodynamic sizes of IONP@LS and IONP@HS changed to 74.1 ± 0.4 nm and 129.3 ± 1.1 nm, respectively. Previous studies indicated that one of the limitations of TEM analysis was that post-evaporation of the liquid medium, the dispersion state of the sample deposited on the copper grid surface might differ from the original state in dispersion solution, especially when an excessive number of NPs with an aggregation were deposited. In contrast, the hydrodynamic size determined via DLS was calculated by measuring the angle and intensity of scattered light within the suspension. It could measure the size of NPs accurately while accounting for potential aggregation. Consequently, it was believed that the protein coronas around NPs, combined with the different degrees of aggregation led to the increased and different DLS results between IONP@LS and IONP@HS. On the other hand, although the hydrodynamic sizes of IONP@LS and IONP@HS increased after exPCs formation, they

remained stable in PBS for up to 3 days, whereas the IONPs increased from 28.0 ± 0.5 nm to 1502.4 ± 173.8 nm within 30 min. Moreover, variations in the hydrodynamic size between IONP@LS and IONP@HS indicated a potential difference in the composition of exPCs. Taken together, these results demonstrated that the formation of exPCs on IONPs substantially promoted their stability in PBS, resulting in better compatibility with the physiological environment in blood.

3.2. Uptake of IONP-exPCs by macrophages

As one of the paramount biological mechanisms, the elimination induced by the mononuclear phagocyte system (MPS) presents the initial hurdle for biomedical NPs upon their introduction into the bloodstream [30]. Adsorption of serum proteins can modulate the blood circulation time of NPs by either accelerating or inhibiting MPS elimination [31,32]. In this regard, we first tested the effect of exPCs on the internalization of IONPs by macrophages. To explore this, we used J774A.1 cell, a mouse macrophage line, to measure the kinetics of IONP@LS and IONP@HS internalization in vitro using LSCM and ICP–OES. Before conducting this, we confirmed that IONPs at a concentration of 20 μg mL^{-1} Fe exhibited negligible cytotoxicity to J774A.1 cells (Fig. S4); therefore, we chose this concentration of IONPs for subsequent experiments.

Initially, the Zeta potential was assessed to evaluate the potential impact of FITC labeling on the physicochemical property of NPs. The findings demonstrated that FITC labeling showed no significantly influence on the physicochemical property of the NPs (Fig. S5). Subsequently, the FITC-labeled NPs were employed for LSCM to investigate

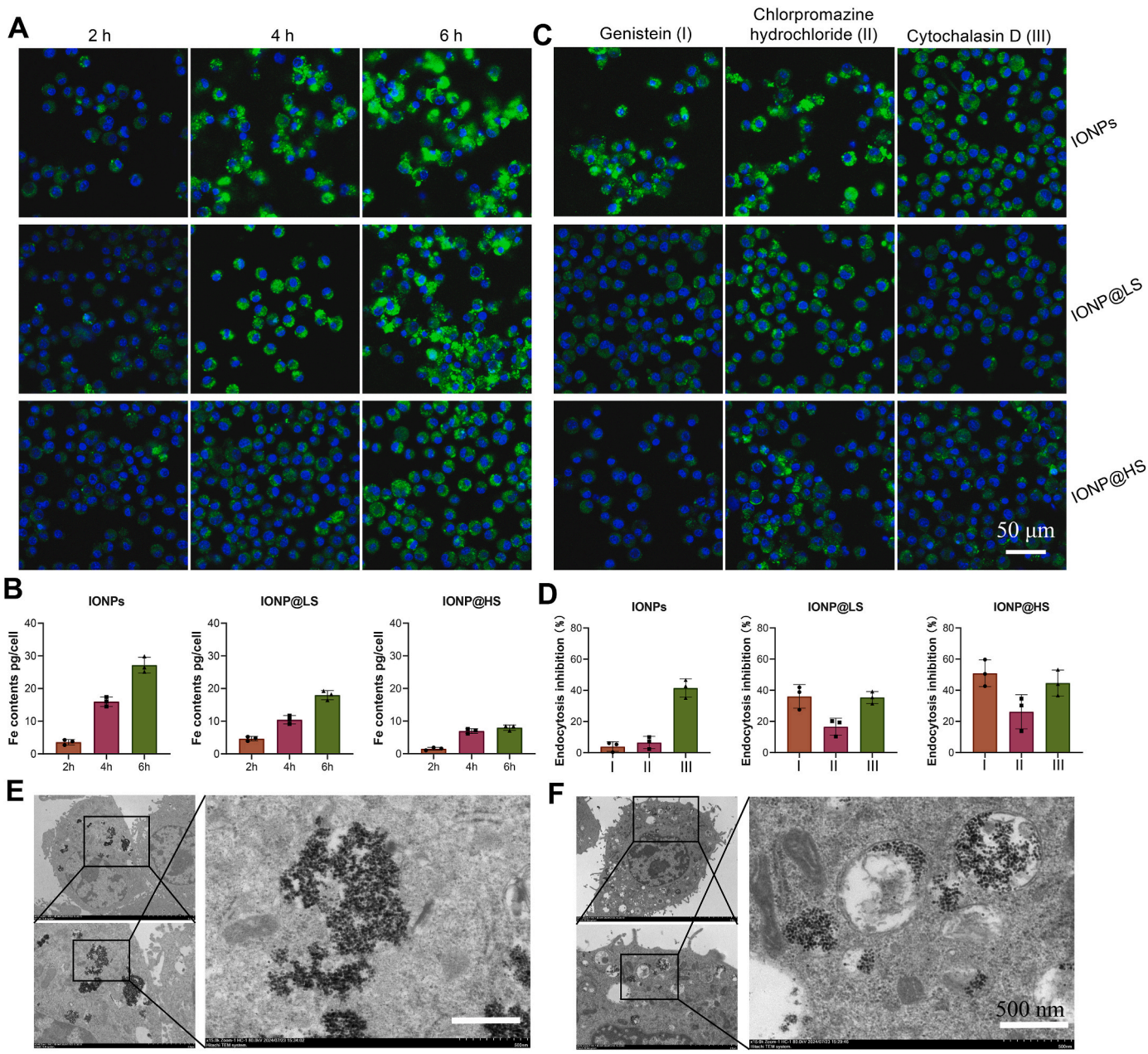

Fig. 2. Effect of exPCs on cellular uptake. (A–B) The LSCM images and Fe content in J774A.1 cells after treatment with IONPs, IONP@LS, or IONP@HS for different durations (2, 4, and 6 h). Green, FITC-labeled NPs; Blue, cell nucleus. (C–D) The LSCM images and Fe content in endocytosis inhibitor pre-treated J774A.1 cells after co-incubation with IONPs, IONP@LS, and IONP@HS for 6 h. I, Genistein pretreatment; II, Chlorpromazine hydrochloride pretreatment; III, Cytochalasin D pretreatment. (E–F) TEM images of J774A.1 cells after IONP@LS (E) and IONP@HS (F) treatment for 6 h, respectively. (For interpretation of the references to colour in this figure legend, the reader is referred to the Web version of this article.)

cellular uptake. As shown in Fig. 2A, the J774A.1 cells treated with IONPs, IONP@LS, and IONP@HS, showed continuous internalization of NPs within 6 h in a time-dependent increasing manner. The most and least uptake at 6 h were observed in IONPs and IONP@HS, respectively. For more accurate quantitative internalization, the Fe contents in cells were measured by ICP−OES (Fig. 2B). IONPs were found to have the highest internalization level (27.2 ± 2.4 pg/cell at 6 h), followed by IONP@LS (18.0 ± 1.4 pg/cell at 6 h), whereas IONP@HS showed the least uptake by J774A.1 cells (8.0 ± 0.8 pg/cell at 6 h). These differential endocytosis profiles confirmed the influence of exPCs on the uptake of IONPs by J774A.1 cells. Furthermore, to verify the internalization of IONPs@LS and IONP@HS, the cells were imaged with TEM and a large number of IONPs were observed inside the cells (Fig. 2E and F).

Besides impacting the internalized contents through exPCs–macrophage interaction, the internalization pathways, which may lead to different intracellular fates of NPs [33,34], can also be influenced by exPCs. Macrophages can internalize allogenic NPs through various ways, such as caveolae-mediated, clathrin-mediated endocytosis, and macropinocytosis. To investigate the effect of exPCs on specific endocytic pathways, three endocytosis inhibitors including genistein, chlorpromazine hydrochloride, and cytochalasin D were utilized to suppress caveolae-mediated endocytosis, clathrin-dependent endocytosis, and macropinocytosis, respectively. As Fig. 2C and D showed, pre-treatment with genistein and chlorpromazine hydrochloride had a negligible effect on the internalization of IONPs (<10 %), as determined by LSCM and ICP−OES. In contrast, there was a significant decrease (*ca.* 41.5 %) in cytochalasin D-pretreated J774A.1 cells, thus revealing macropinocytosis as the primary internalization pathway for IONPs. Regarding IONP@LS, a conspicuous decrease in green fluorescence could be observed in cells treated with all three inhibitors, with genistein, chlorpromazine hydrochloride, and cytochalasin D causing 36.0 %, 16.6 %, and 35.3 % decreases in endocytosis, respectively. This indicated the involvement of multiple endocytosis pathways for IONP@LS, primarily caveolae-mediated endocytosis and macropinocytosis. IONP@HS showed the least green fluorescence compared with IONPs and IONP@LS, and displayed much stronger inhibition rates than IONP@LS by corresponding inhibitors. Taken together, these results highlighted the differences in the internalization content and internalization pathway between IONP@LS and IONP@HS by macrophages, indicating exPCs have significant influences on NPs–cytomembranes interactions.

3.3. Identification of exPCs

Previous studies have indicated the crucial role of protein component of exPCs in mediating cell–NP interactions; therefore, identification of the protein composition of exPCs may contribute to understanding the mechanism of internalization differences. Here, the protein contents around the IONP-exPCs were first analyzed quantitatively, and approximately 0.67 ± 0.12 μg and 1.06 ± 0.26 μg of protein per μg of Fe were detected in the IONP@LS and IONP@HS, respectively. Then, SDS−PAGE was employed to analyze the protein composition of exPCs surrounding the IONPs by loading the same amount of the IONP–exPCs complexes with the same amount of Fe. As shown in Fig. 3A, IONP@LS and IONP@HS showed distinct distribution patterns of proteins depending on molecular weight, suggesting differences in protein species and contents between the two corona formations.

Subsequently, LC−MS/MS was used to investigate the protein compositions of the two aforementioned exPCs. Principal component analysis (PCA) revealed two distinct clusters, indicating a significant difference in protein composition between IONP@LS and IONP@HS and indicating reliable biological repeatability in each group (Fig. 3B). Then, the different expressed proteins identified in IONP@LS and IONP@HS were visualized using a heat-map (Fig. 3C) and volcano plot (Fig. 3D), from which 131 proteins with higher abundance and 91 proteins with lower abundance were identified in IONP@HS than in IONP@LS. The top 20 varied proteins (11 with higher abundance, 9 with lower abundance) were identified and listed in Table S2. From which, we noticed that many of these differential proteins were associated with complement or immune response, such as complement factor B (cfb) and immunoglobulin kappa chain variable 7–33 (Igkv7-33), which belong to opsonin-related proteins and could be recognized by macrophages to accelerate the internalization of NPs [18], the differences in opsonin and dysopsonin proteins between these two exPCs were then analyzed comprehensively (Fig. 3E). We found opsonin-dominated and dysopsonin-lacking protein components in IONP@LS, which explained the higher internalization of IONP@LS than IONP@HS by macrophages. Besides the difference in opsonin proteins, a greater abundance of albumin (Alb, which can bind to gp60, a receptor involved in caveolae-mediated endocytosis) was identified in IONP@HS (Fig. 3C), which may be in charge of the higher caveolae-mediated endocytosis inhibition for IONP@HS (Fig. 2C and D). Meanwhile, the lipoproteins Apob, Apoa2, Apoa3, Apoa4, Apoa5, and Apoc1 also existed significant differences in content between IONP@HS and IONP@LS (Fig. 3D), which could lead to distinct internalization efficiencies by *LDLR*-rich hepatocytes (This was confirmed in the following testing).

In addition to influencing the uptake by cells, variations in exPCs could also engender additional biological consequences. To discern these potential biological impacts, an enrichment analysis of gene ontology (GO) was executed utilizing the differential proteins to gain a deeper understanding of the multifaceted characteristics of genes and their respective biological effects. As shown in Fig. 3F and G, the GO enrichment analysis revealed that the exPCs formed at these two different protein concentrations result in differential biological processes such as the morphogenesis of branching epithelia, acute inflammatory responses, and membrane lipid metabolism, and in molecular functions such as icosanoid binding, fatty acid derivative binding, and CXCR chemokine receptor binding. Among these different items, we noted that CXCR chemokine receptor binding, a receptor over-expressed in tumor cells that recognized Cxcl5 [35], showed greater enrichment in IONP@HS than in IONP@LS, indicating IONP@HS may have a better tumor cell targeting capacity than IONP@LS and that this was confirmed by an internalization experiment in 4T1 cells (Fig. S6).

Overall, these findings confirmed that the different components of exPCs contributed to the differences in MPS-related internalization and tumor cell targeting capacity. The reduced tumor cell targeting capacity and increased MPS clearance of IONP@LS could lead to an incorrect in vitro evaluation of the accumulation of IONPs in tumors.

3.4. LDLR-mediated hepatocyte uptake of IONP-exPCs

Based on the proteomic analysis presented in Fig. 3D, a notable dissimilarity in lipoprotein content was found between the two IONP-exPCs complexes. Previous studies have indicated that hepatocytes play a central role in the clearance of exogenous NPs, especially lipidosome-associated or lipoprotein-coated NPs [36]. Lipoproteins, consisting of lipid and protein components, were found in plasma and frequently adsorbed by NPs to compose exPCs. For instance, as shown in Fig. 3D, the lipoproteins Apob, Apoa2, Apoa4, and Apoc1 were identified with a lower abundance in IONP@HS than in IONP@LS. *LDLR*, a receptor that could recognize and mediate the endocytosis of lipoproteins, particularly Apob, into hepatocytes, thereby decreasing the lifetime of systemic circulation through the acceleration of hepatic clearance. To elucidate the influence of exPCs on hepatocyte uptake and underlying mechanism, AML12 mouse hepatocyte cell line was employed. After co-incubation with AML12 cells in serum-free conditions, IONP@HS-treated cells showed significantly less blue pigment than IONP@LS-treated cells (Fig. 4C, the control group). To identify the reason for this difference in endocytosis efficiency, two different concentrations of *LDLR*-siRNA were used to knock down *LDLR* expression to generate two genetically edited AML12 cells with medium or low *LDLR*

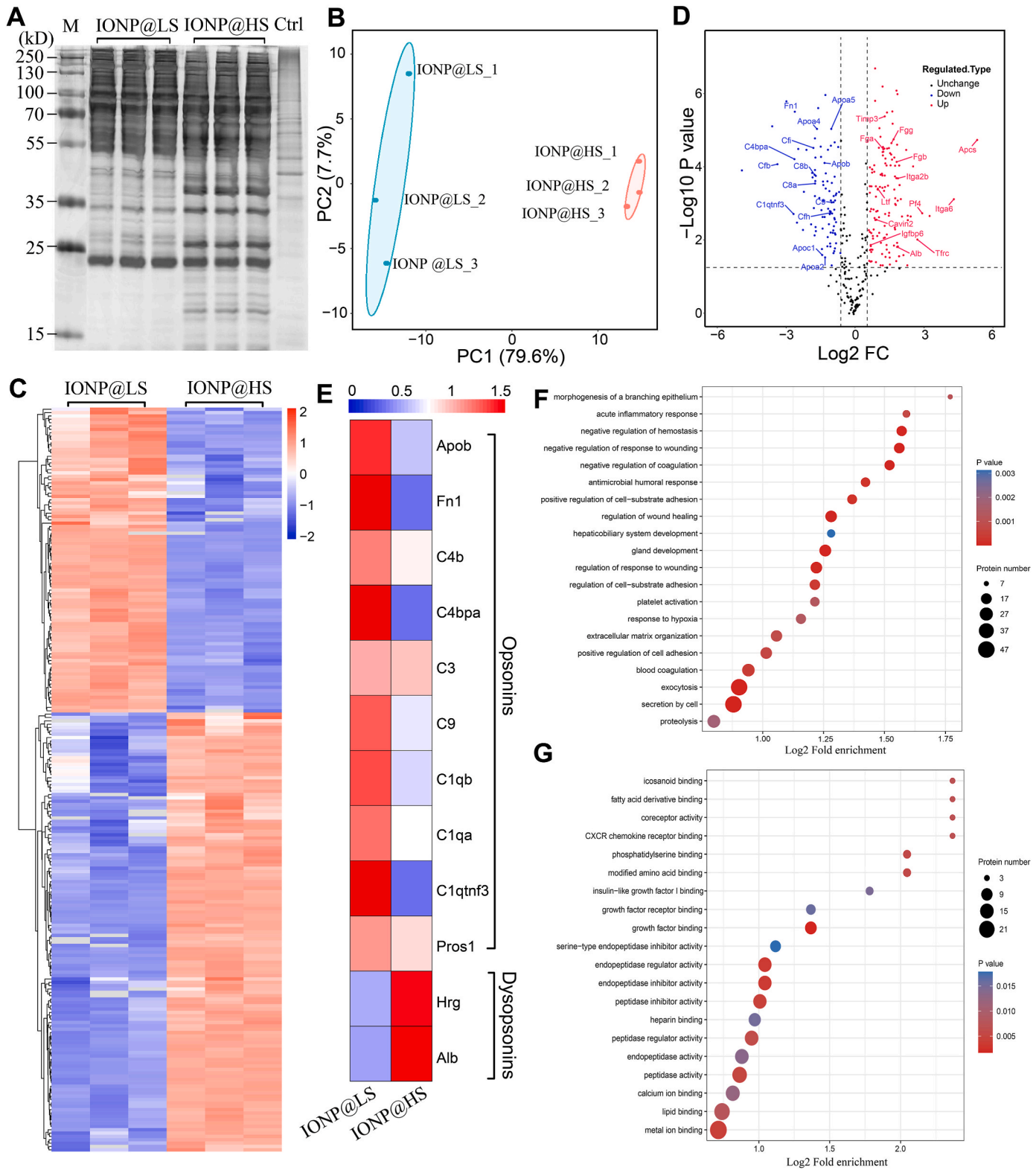

Fig. 3. Proteomic analysis of the extracellular protein corona. (A) SDS–PAGE analysis of IONP@LS and IONP@HS. M, protein mark; Ctrl, cell total proteins. (B) PCA scatter plot of proteomic data. (C–D) Heat-map and volcano plot of identified differentially expressed proteins. (E) Heat-map showing differences in the abundance of some identified opsonin and dysopsonin proteins between IONP@LS and IONP@HS. (F–G) Biological process and molecular function-based GO enrichment analysis of the up-regulated proteins identified in the IONP@HS group compared with the IONP@LS group.

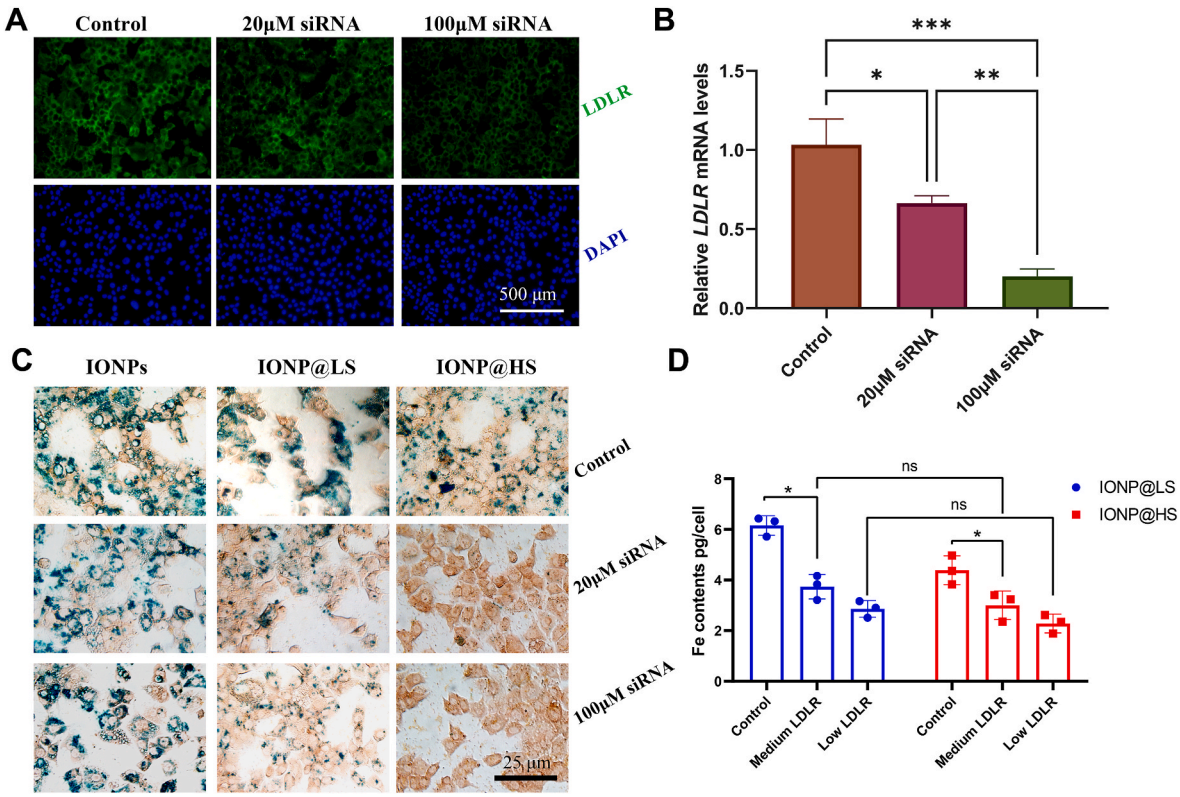

Fig. 4. Effect of exPCs on the uptake of IONPs by AML12 cells. (A) Immunofluorescence analysis of *LDLR* expression in siRNA-treated AML12 cells. Green, *LDLR*; Blue, cell nucleus. (B) Relative *LDLR* mRNA levels in siRNA-treated AML12 cells. (C) Prussian blue staining of AML12 cells after treatment with IONPs, IONP@LS, or IONP@HS for 6 h. Blue: intracellular Fe; Brown: cytoplasm. (D) Fe contents in AML12 cells after treatment with IONPs, IONP@LS, or IONP@HS. (For interpretation of the references to colour in this figure legend, the reader is referred to the Web version of this article.)

levels, which were confirmed by immunofluorescence staining and qRT−PCR analysis (Fig. 4A and B). After treatment with IONP@LS or IONP@HS for 6 h, normal AML12 cells exhibited the most blue pigment (the control group), whereas AML12 cells with medium or low *LDLR* levels demonstrated decreased uptake of IONP@LS and IONP@HS (Fig. 4C). Furthermore, the Fe contents in different AML12 cells were analyzed by ICP–OES (Fig. 4D). Compared with those of control cells, significantly reduced internalization contents of IONP@LS and IONP@HS were observed in siRNA-treated cells, but no significant difference was detected between IONP@LS and IONP@HS in *LDLR*-knockdown cells ($p > 0.05$), which further underscored the role of *LDLR* in mediating the uptake of IONP@LS and IONP@HS. These findings confirmed that the difference in the lipoprotein content of exPCs was responsible for the difference in hepatocyte clearance between IONP@LS and IONP@HS.

Collectively, these discoveries suggested that exPCs, formed in different biofluids, may instigate differential internalization rates of IONPs by macrophages or hepatocytes via specific protein species such as Fn1, C4b, Alb, and Apob.

3.5. Transcriptome analysis of intracellular biological effects

While previous studies have emphasized the potential of exPCs to mediate nano–cytomembrane interface reactions, there has been limited research on their impacts on intracellular biological outcomes. To determine the impact of initial exPCs on intracellular physiological behaviors, whole-transcriptome sequencing (RNA-seq), an effective methodology for delineating genome-wide changes in gene expression, was used to analyze mRNA expression patterns. As the main components of the MPS, macrophages were well-known target cells in NPs-based inflammatory therapy and cancer treatment, among others. Hence, J774A.1 cells were also used as model cells to explore the potential differences in the intracellular biological effects of IONP@LS and IONP@HS.

The Pearson's correlation coefficient for each group was found more than 0.99 (Fig. S7), indicating a high level of repeatability. Then, a differential gene clustering heat-map was constructed to visualize the gene expression profiles of the cells exposed to IONPs, IONP@LS, and IONP@HS and control cells (Fig. 5A). IONPs-treated cells exhibited an expression pattern that was more similar to that of blank control cells, whereas the expression patterns of IONP@LS and IONP@HS were more similar. The numbers of differentially expressed genes in different comparisons were determined and shown in Fig. 5B. Compared with IONPs, the formation of exPCs significantly increased the number of differentially expressed genes. The largest difference was observed between the IONP@HS and control cells, indicating that the formation of exPCs around IONPs in a high-protein environment may have a greater influence on the intracellular biological effect. Although only 58 differentially expressed genes were identified between the IONP@LS and IONP@HS treatments (Fig. 3C), this finding indicated that exPCs with different compositions can induce distinct intracellular biological effects.

To elucidate the regulatory effects of the two exPCs on functional gene sets, gene set enrichment analysis (GSEA) was performed to investigate alterations in enriched signaling pathways between IONP@LS and IONP@HS treatment. As shown in Figs. S8A and B, complement activation and immune response signaling pathways, which played critical roles in the regulation of physiological and pathological reactions such as bacteriolytic and cytotoxic effects, were down-regulated in IONP@HS-treated J774A.1 cells compared with IONP@LS-treated cells. The mRNA levels of complement component 1 (*C1S1*) and aconitate decarboxylase 1 (*ACOD1*) in IONP@HS- and IONP@LS-treated J774A.1 cells were analyzed and displayed in Fig. S9. *C1S1* encoded a serine protease, which was a major component in complement

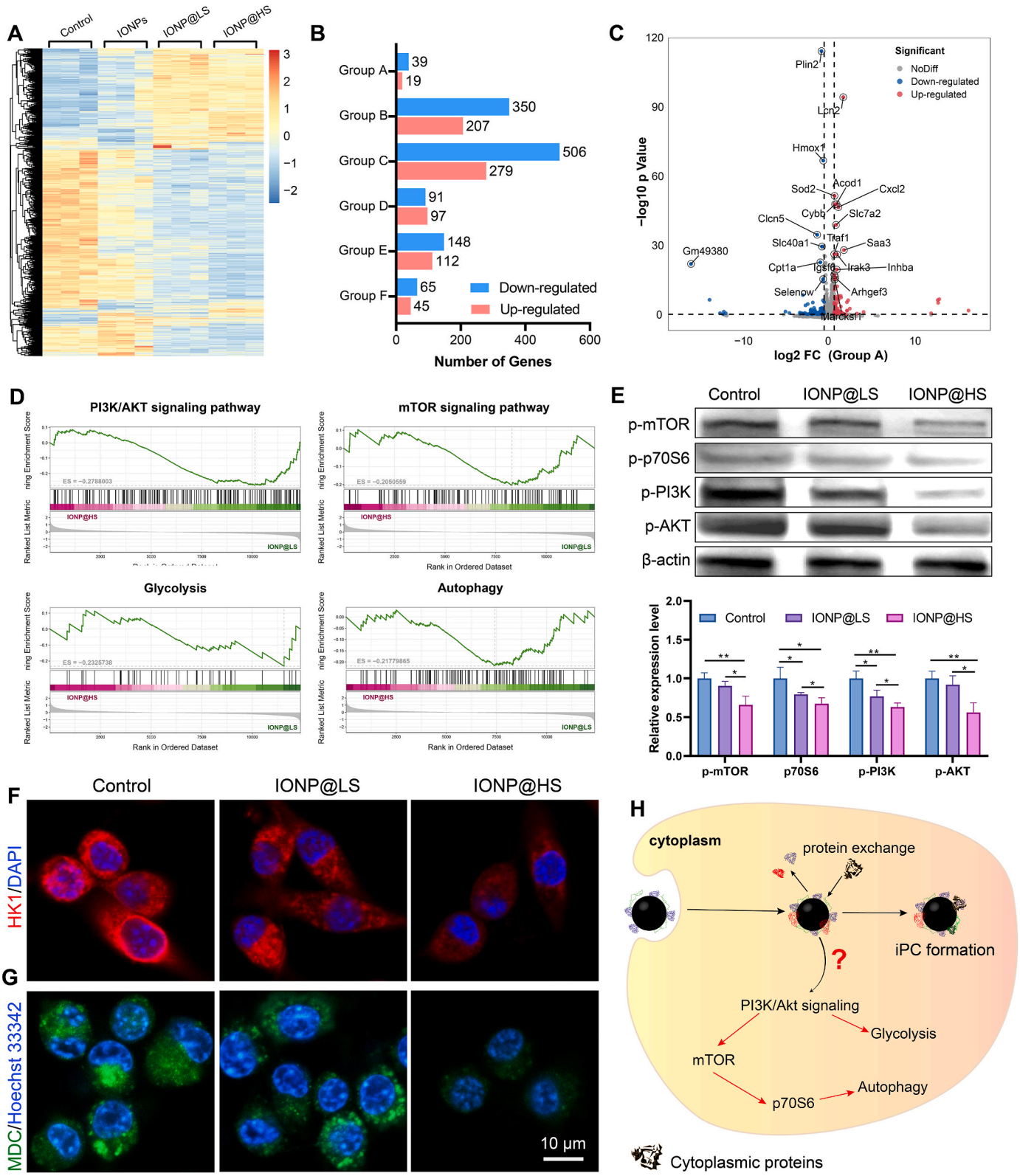

Fig. 5. Transcriptome analysis of J774A.1 cells. (A) Heatmap showing the expression patterns of genes in J774A.1 cells after different treatments. Control: J774A.1 cells; IONPs: IONPs treated J774A.1 cells; IONP@LS: IONP@LS treated J774A.1 cells; IONPs@HS: IONPs@HS treated J774A.1 cells. (B) Number of different genes identified in different groups: Group A, IONP@HS versus IONP@LS; Group B, IONP@LS versus Control; Group C, IONP@HS versus Control; Group D, IONP@LS versus IONPs; Group E, IONP@HS versus IONPs; Group F, IONPs versus Control. (C) Volcano map of identified differential genes in Group A (IONP@HS versus IONP@LS). (D) Biological process-based GSEA for the PI3K/AKT signaling pathway, mTOR signaling pathway, glycolysis and autophagy in Group A (IONP@HS versus IONP@LS). (E) Western blot analysis of the expression of p-mTOR, p-p70S6, p-PI3K, and p-AKT in IONP@LS- and IONP@HS-treated cells. (F) Immunofluorescence analysis of HK1 expression in IONP@LS- and IONP@HS-treated cells. Red: HK1; Blue: cell nucleus. (G) MDC-based autophagy staining of IONP@LS- and IONP@HS-treated cells. Green: MDC; Blue: cell nucleus. (H) Schematic diagram of the intracellular metabolic changes induced by exPCs. (For interpretation of the references to colour in this figure legend, the reader is referred to the Web version of this article.)

subcomponent C1, and we identified a down-regulation in IONP@HS-treated cells compared with IONP@LS-treated cells, which was consistent with the GSEA results (Fig. S8A). The ACOD1 protein acted as a negative regulator of the Toll-like receptor-mediated inflammatory response. We identified a significant increase in *ACOD1* mRNA in IONP@HS-treated cells ($p < 0.01$), which was also shown in Fig. 5C, combined with the decreased *C1S1* mRNA, indicating the down-regulation of the immune response in IONP@HS-treated cells, which was also consistent with the GSEA results (Fig. S8B). In addition, the cells subjected to IONP@HS treatment also exhibited a down-regulated expression pattern in relation to caveolae and phagocytosis (Figs. S8C and D), suggesting that IONP@HS-treated J774A.1 cells exhibited weaker internalization than IONP@LS-treated cells, which was verified by an uptake assay (Fig. S10).

In addition to the above-mentioned common impacts, some specific biological processes were also enriched in the present study. As shown in Fig. 5D, the PI3K/AKT and mTOR signaling pathways showed decreased expression levels in IONP@HS-treated J774A.1 cells compared with IONP@LS-treated cells. The PI3K/AKT and mTOR signaling pathways played key roles in numerous physiological activities in cells, and according to GSEA, glycolysis and autophagy were involved. To verify these changes in biological behaviors, western blotting analysis was used to test the expression levels of p-mTOR, p-PI3K, and p-AKT. As shown in Fig. 5E, all the tested proteins in cells treated with IONP@LS and IONP@HS were decreased compared with those in control cells, and IONP@HS treatment induced the lowest protein levels, which confirmed the GSEA results. To further evaluate glycolysis and autophagy activity in IONP@LS- and IONP@HS-treated cells, hexokinase 1 (HK1)-based immunofluorescence staining and MDC-based autophagy staining were conducted, and the results were shown in Fig. 5F and G. As expected, the cells treated with IONP@HS displayed weaker fluorescence intensity than IONP@LS-treated cells, and the strongest fluorescence intensity was detected in the control cells. Therefore, we concluded that IONP@LS and IONP@HS treatment resulted in differences in glycolysis and autophagy, mainly through changes in the PI3K/AKT-mTOR signaling pathway. Previous studies have shown that mTOR often inhibits autophagy through the classical autophagy-related 13 pathway, but both mTOR and autophagy decreased in IONP@HS, indicating that a non-classical pathway may be involved, such as p70S6-mediated autophagy with a feedback model [37], which was confirmed in Fig. 5E. A schematic of the exPCs-induced glycolysis and autophagy through the PI3K/AKT-mTOR signaling pathway was shown in Fig. 5H. However, the mechanism of exPCs-induced differences in glycolysis and autophagy needed further exploration.

3.6. The evolution of exPCs after internalization contributes to metabolic behaviors

For most biomedical NPs, they work mainly at subcellular locations. As the intracellular environment differs dramatically from the extracellular environment, and once internalized, NPs may be subject to exchange with native intracellular proteins, leading to the evolution of exPCs and interference with intracellular proteostasis, thus contributing to the different metabolisms in cells.

Predominantly, NPs underwent the endosome–lysosome route of intracellular trafficking, where they eventually permeated into the cytoplasm or subcellular organelle to exert their pharmacological functions or be transported outside via secretory vesicles. Therefore, as an initial step, we analyzed the evolution of exPCs during the biological process of intracellular transport. While the extraction of IONPs–iPCs complexes from intracellular environments post-NPs treatment might yield more precise results, the separation procedures could introduce a range of chemicals, including cell lysate, potentially resulting in the modification of PCs. Hence, we simulated the intracellular transport process of NPs in vitro, which was a universally recognized method under current technical conditions. Fig. S11 illustrated the incubation workflow of the two exPCs-coated IONPs (IONP@LS and IONP@HS) with sequential lysosomal and cytoplasmic proteins to simulate intracellular transport, resulting in the formation of new protein-coated IONPs (denoted as IONP@LSC and IONP@HSC, respectively).

The proteins in IONP@LSC and IONP@HSC were initially characterized using SDS−PAGE analysis. IONP@LSC and IONP@HSC showed partial differences in brightness for specific protein bands, suggesting differences in the abundance for these proteins (Fig. 6A). Subsequently, label-free LC−MS/MS was used to quantitatively analyze these differences. As presented in Fig. S12, the IONP@LSC and IONP@HSC groups showed two discernible clusters with obvious differences in the PCA scatter plot. Then, the up-regulated and down-regulated proteins in the different comparison groups were analyzed (Fig. 6B). Specifically, 76 and 82 proteins were found to be up- and down-regulated in IONP@LSC compared with those in IONP@LS (Group I), suggesting the exchange of proteins in IONP@LS during incubation with lysosomal and cytoplasmic proteins. Interestingly, many more differences were identified between IONP@HSC and IONP@HS (Group II), suggesting more pronounced intracellular protein exchange in IONP@HS than in IONP@LS. For the comparison of IONP@HSC and IONP@LSC (Group III), we discerned a total of 184 different proteins and generated a heat-map (Fig. 6B and C). The number of these differential proteins was notably less than that observed in exPCs (which comprised 222 proteins). This suggests that the uniform intracellular environment during the internalization of NPs mitigates the disparities in the composition of exPCs that originate from varying extracellular environments.

To gain further insight into the impact of differential proteins on specific functional pathways, particularly the observed differences in the PI3K/AKT–mTOR signaling pathway, glycolysis, and autophagy, a comprehensive analysis of these differentially-enriched proteins was undertaken. From which, the angiopoietin 1 (Ang 1) was identified and showed a significant difference between IONP@HSC and IONP@LSC, which may potentially contribute to the observed variations in PI3K/AKT–mTOR, and glycolysis and autophagy [38,39]. To verify the difference in Ang 1 content between IONP@HSC and IONP@LSC, the two complexes were analyzed by western blotting and the results were showed in Fig. 6E. Significantly more Ang 1 protein was found in IONP@HSC. To further confirm the more depletion of Ang 1 after IONP@HS treatment, the PCs formed in lysosomes were also analyzed, and the relative variation in Ang 1 content from lysosomes to cytoplasm was showed in Fig. S13. Elevated level of Ang 1 was detected in IONP@HSC, suggesting a greater depletion of intracellular Ang 1 following IONP@HS treatment. This finding was corroborated by quartz crystal micro-balance analysis, which demonstrated that Ang 1 exhibited a greater binding affinity to IONP@HS than to IONP@LS (Fig. S14). The precise mechanisms underlying this enhanced affinity between Ang 1 and IONP@HS, potentially involving protein–protein interactions, electrostatic interactions, and hydrogen bonding, among other factors, remain unclear. Although previous studies have shown that Ang 1 plays an important regulatory role in the PI3K/AKT–mTOR signaling pathway, the PI3K/AKT–mTOR signaling pathway may be regulated by other stimulations, like starvation. Hence, to test the effect of Ang 1 depletion on the PI3K/AKT–mTOR signaling pathway, the Ang 1-over--expressing J774A.1 (J774A.1$^{Ang\ 1+}$) cells were established through the transfection of Ang 1 over-expressing plasmids (Fig. 6F). Subsequently, these J774A.1$^{Ang\ 1+}$ cells were treated with IONP@LS and IONP@HS, followed by an analysis of the PI3K/AKT–mTOR signaling pathway. As shown in Fig. 6G and H, there were no significant differences in any of the tested proteins between the IONP@LS and IONP@HS groups, which proved the difference in the depletion of Ang 1 contributed to the varied PI3K/AKT–mTOR signalings. Furthermore, the autophagy and glycolysis also showed no significant difference between the IONP@LS and IONP@HS treated J774A.1$^{Ang\ 1+}$ cells (Fig. 6I and J). These results confirmed that greater depletion of Ang 1 by IONP@HS contributed to the decreased PI3K/AKT–mTOR signaling, ultimately resulting in different autophagy and glycolysis activities.

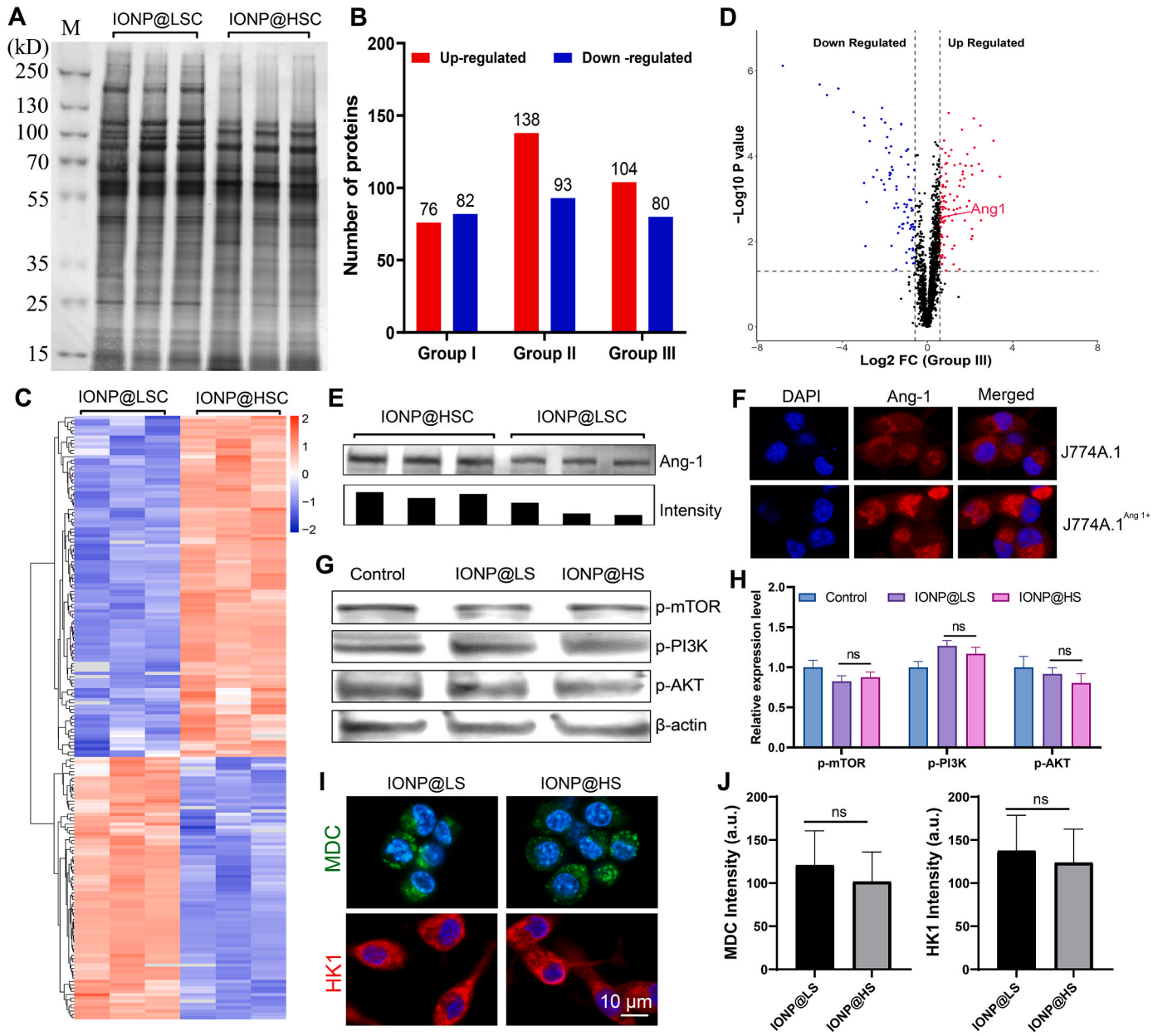

Fig. 6. Evolution of the extracellular protein corona during internalization and the mechanism of metabolic differences. (A) SDS–PAGE analysis of IONP@LSC and IONP@HSC. (B) Number of different proteins identified in different groups: Group I, IONP@LSC versus IONP@LS; Group II, IONP@HSC versus IONP@HS; Group III, IONP@HSC versus IONP@LSC; (C–D) heat-map and volcano plot of identified differential proteins. (E) Western blot analysis of Ang 1 levels in IONP@HSC and IONP@LSC. (F) Immunofluorescence analysis of the expression level of Ang 1 in cells after plasmid transfection. (G–H) Western blot analysis of p-mTOR, p-p70S6, p-PI3K, and p-AKT in IONP@LS- and IONP@HS-treated J774A.1^{Ang1+} cells. (I) Immunofluorescence analysis of HK1 expression and MDC-based autophagy staining in IONP@LS- and IONP@HS-treated J774A.1^{Ang1+} cells. Blue: cell nucleus; Green: MDC; Red: HK1. (J) Fluorescence intensity of HK1 and autophagy in J774A.1^{Ang1+} cells. (For interpretation of the references to colour in this figure legend, the reader is referred to the Web version of this article.)

To summarize, proteomic analysis of iPCs formed during the simulated endocytosis process of IONPs confirmed the dynamic exchange of proteins between the original exPCs and intracellular proteins. Furthermore, the difference in protein exchange of IONP@LS and IONP@HS led to varied autophagy and glycolysis activities through PI3K/AKT–mTOR signaling by the depletion of intracellular Ang 1.

4. Conclusions

In this study, two exPCs-coated IONPs were synthesized and their biological impacts on both extracellular and intracellular were evaluated comprehensively. The proteomic analysis of the two exPCs revealed that the proteins presented in exPCs significantly impact the interactions between IONPs and cytomembranes, a finding that aligned with the results of numerous previous studies. Significantly, our research revealed that distinct exPCs can stimulate diverse glycolysis and autophagy activities following their uptake by J774A.1 cells. Futher proteomic analysis of iPCs indicated that the increased Ang 1 content in IONP@HSC was responsible for the differences in autophagy and glycolysis activities due to different depletion of intracellular Ang 1. In summary, this study offers a potential explanation for the varying biological effects of NPs in different biological environments and guides the design of NPs and reasonable analysis of results in various biological environments, ultimately accelerating the clinical application of biomedical NPs.

CRediT authorship contribution statement

Liang Zhang: Writing – review & editing, Writing – original draft, Validation, Methodology, Investigation, Funding acquisition, Formal analysis, Data curation, Conceptualization. **Tao Sun:** Methodology, Investigation. **Mingfu Gong:** Writing – review & editing, Validation, Funding acquisition, Conceptualization. **Chunyu Zhou:** Investigation. **Yue Zhao:** Investigation. **Wansu Zhang:** Investigation. **Zhipeng Zhang:** Investigation. **Shilin Xiao:** Investigation. **Xiaofeng Yang:** Investigation. **Miaomiao Wang:** Investigation. **Xu Liu:** Investigation. **Qian Xie:** Investigation. **Dong Zhang:** Writing – review & editing, Validation, Supervision, Project administration, Funding acquisition, Conceptualization.

Declaration of competing interest

The authors declare that they have no known competing financial interests or personal relationships that could have appeared to influence the work reported in this paper.

Data availability

Data will be made available on request.

Acknowledgments

This work was supported by National Natural Science Foundation of China (32301196, 82372030), Natural Science Foundation of Chongqing (cstc2021jcyj-msxmX1093, cstc2022ycjh-bgzxm0082, CSTB2022NSCQ-MSX0763), the Talent Project of Chongqing (CQYC202103075), the Chongqing Young and Middle-aged Medical High-end Talent project (Mingfu Gong), and Miaopu Foundation of Army Medical University (No. 2019R059, Liang Zhang).

Appendix A. Supplementary data

Supplementary data to this article can be found online at https://doi.org/10.1016/j.mtbio.2024.101215.

References

[1] M. Sharma, P. Alessandro, S. Cheriyamundath, M. Lopus, Therapeutic and diagnostic applications of carbon nanotubes in cancer: recent advances and challenges, J. Drug Target. 32 (3) (2024) 287–299.
[2] W.F. Zeng, Z.M. Li, Q.L. Huang, C.D. Ding, L. Yang, W.Y. Wang, et al., Multifunctional mesoporous polydopamine-based systematic delivery of STING agonist for enhanced synergistic photothermal-immunotherapy, Adv. Funct. Mater. 34 (2024) 2307241.
[3] Q.Q. Bai, Y. Xiao, H.L. Hong, X.Y. Cao, L. Zhang, R.F. Han, et al., Scavenger receptor-targeted plaque delivery of microRNA-coated nanoparticles for alleviating atherosclerosis, P Natl Acad Sci 119 (39) (2022) e2201443119.
[4] L. Zhang, X.Y. Tian, C.K.W. Chan, Q.Q. Bai, C.K. Cheng, F.M. Chen, et al., Promoting the delivery of nanoparticles to atherosclerotic plaques by DNA coating, Acs Appl Mater Inter 11 (15) (2019) 13888–13904.
[5] J.C. Pessa, J. Joutsen, L. Sistonen, Transcriptional reprogramming at the intersection of the heat shock response and proteostasis, Mol Cell 84 (1) (2024) 80–93.
[6] F. Guo, S. Luo, L. Wang, M. Wang, F. Wu, Y. Wang, et al., Protein corona, influence on drug delivery system and its improvement strategy: a review, Int. J. Biol. Macromol. 256 (2) (2024) 128513.
[7] W.H. Wang, H.H. Liu, Z.W. Huang, F.Q. Fu, W.H. Wang, L.J. Wu, et al., The effect of organic ligand modification on protein corona formation of nanoscale metal organic frameworks, Chin. Chem. Lett. 33 (9) (2022) 4185–4190.
[8] W.C. Chou, Z. Lin, Impact of protein coronas on nanoparticle interactions with tissues and targeted delivery, Curr. Opin. Biotechnol. 85 (2023) 103046.
[9] S. Vranic, I. Gosens, N.R. Jacobsen, K.A. Jensen, B. Bokkers, A. Kermanizadeh, et al., Impact of serum as a dispersion agent for in vitro and in vivo toxicological assessments of TiO_2 nanoparticles, Arch. Toxicol. 91 (1) (2017) 353–363.
[10] W. Wang, Z. Huang, Y. Li, W. Wang, J. Shi, F. Fu, et al., Impact of particle size and pH on protein corona formation of solid lipid nanoparticles: a proof-of-concept study, Acta Pharm. Sin. B 11 (4) (2021) 1030–1046.
[11] M. Xu, Y. Qi, G. Liu, Y. Song, X. Jiang, B. Du, Size-dependent in vivo transport of nanoparticles: implications for delivery, targeting, and clearance, ACS Nano 17 (21) (2023) 20825–20849.
[12] K. Girigoswami, P. Pallavi, A. Girigoswami, Intricate subcellular journey of nanoparticles to the enigmatic domains of endoplasmic reticulum, Drug Deliv. 30 (1) (2023) 2284684.
[13] S. Subramaniam, P. Joyce, L. Donnellan, C. Young, A. Wignall, P. Hoffmann, et al., Protein adsorption determines pulmonary cell uptake of lipid-based nanoparticles, J. Colloid Interface Sci. 641 (2023) 36–47.
[14] S. Khan, M. Sharifi, J.P. Gleghorn, M.M.N. Babadaei, S.H. Bloukh, Z. Edis, et al., Artificial engineering of the protein corona at bio-nano interfaces for improved cancer-targeted nanotherapy, J Control Release 348 (2022) 127–147.
[15] X. Yang, L. Cheng, Y. Zhao, H. Ma, H. Song, X. Yang, et al., Aggregation-induced emission-active iridium (III)-based mitochondria-targeting nanoparticle for two-photon imaging-guided photodynamic therapy, J Colloid Interf Sci 659 (2024) 320–329.
[16] M. Cao, R. Cai, L. Zhao, M. Guo, L. Wang, Y. Wang, et al., Molybdenum derived from nanomaterials incorporates into molybdenum enzymes and affects their activities in vivo, Nat. Nanotechnol. 16 (6) (2021) 708–716.
[17] R. da Costa Marques, N. Hüppe, K.R. Speth, J. Oberländer, I. Lieberwirth, K. Landfester, et al., Proteomics reveals time-dependent protein corona changes in the intracellular pathway, Acta Biomater. 172 (2023) 355–368.
[18] M.J. Cao, R. Cai, L.N. Zhao, M.Y. Guo, L.M. Wang, Y.C. Wang, et al., Molybdenum derived from nanomaterials incorporates into molybdenum enzymes and affects their activities in vivo, Nat. Nanotechnol. 16 (6) (2021) 708–716.
[19] M. Guo, L. Zhao, J. Liu, X. Wang, H. Yao, X. Chang, et al., The underlying function and structural organization of the intracellular protein corona on graphdiyne oxide nanosheet for local immunomodulation, Nano Lett. 21 (14) (2021) 6005–6013.
[20] M. Qin, J. Zhang, M. Li, D. Yang, D. Liu, S. Song, et al., Proteomic analysis of intracellular protein corona of nanoparticles elucidates nano-trafficking network and nano-bio interactions, Theranostics 10 (3) (2020) 1213–1229.
[21] T. Sun, Y.D. Liu, C.Y. Zhou, L. Zhang, X. Kang, S.L. Xiao, et al., Fluorine-mediated synthesis of anisotropic iron oxide nanostructures for efficient T-2-weighted magnetic resonance imaging, Nanoscale 13 (16) (2021) 7638–7647.
[22] R. Cai, J. Ren, M. Guo, T. Wei, Y. Liu, C. Xie, et al., Dynamic intracellular exchange of nanomaterials' protein corona perturbs proteostasis and remodels cell metabolism, Proc Natl Acad Sci 119 (23) (2022) e2200363119.
[23] Z.H. Zhao, M.Y. Li, J. Zeng, L.L. Huo, K. Liu, R.X. Wei, et al., Recent advances in engineering iron oxide nanoparticles for effective magnetic resonance imaging, Bioact. Mater. 12 (2022) 214–245.
[24] C.S. Nascimento, E.A.R. Alves, C.P. de Melo, R. Correa-Oliveira, C.E. Calzavara-Silva, Immunotherapy for cancer: effects of iron oxide nanoparticles on polarization of tumor-associated macrophages, Nanomedicine 16 (29) (2021) 2633–2650.
[25] S.H. Noh, S.H. Moon, T.H. Shin, Y. Lim, J. Cheon, Recent advances of magneto-thermal capabilities of nanoparticles: from design principles to biomedical applications, Nano Today 13 (2017) 61–76.
[26] D. Cao, X.Y. Jin, L. Gan, T. Wang, Z.L. Chen, Removal of phosphate using iron oxide nanoparticles synthesized by eucalyptus leaf extract in the presence of CTAB surfactant, Chemosphere 159 (2016) 23–31.
[27] X. Li, E.R. He, B. Xia, Y. Liu, P.H. Zhang, X.D. Cao, et al., Protein corona-induced aggregation of differently sized nanoplastics: impacts of protein type and concentration, Environ. Sci.: Nano 8 (6) (2021) 1560–1570.
[28] L.F. Ferreira, A.S. Picco, F.E. Galdino, L.J.C. Albuquerque, J.-F. Berret, M. B. Cardoso, Nanoparticle–protein interaction: demystifying the correlation between protein corona and aggregation phenomena, ACS Appl. Mater. Interfaces 14 (25) (2022) 28559–28569.
[29] G.K. Wang, W.L. Wang, E. Shangguan, S.Y. Gao, Y.F. Liu, Effects of gold nanoparticle morphologies on interactions with proteins, Mater Sci Eng C-Mater Biol Appl 111 (2020) 110830.
[30] R. Bodoque-Villar, D. Padilla-Valverde, L.M. Gonzalez-Lopez, J.R. Munoz-Rodriguez, J. Arias-Pardilla, C. Villar-Rodriguez, et al., The importance of CXCR4 expression in tumor stroma as a potential biomarker in pancreatic cancer, World J. Surg. Oncol. 21 (1) (2023) 287.
[31] S. Ritz, S. Schottler, N. Kotman, G. Baier, A. Musyanovych, J. Kuharev, et al., Protein corona of nanoparticles: distinct proteins regulate the cellular uptake, Biomacromolecules 16 (4) (2015) 1311–1321.
[32] S.M. Pustulka, K. Ling, S.L. Pish, J.A. Champion, Protein nanoparticle charge and hydrophobicity govern protein corona and macrophage uptake, ACS Appl. Mater. Interfaces 12 (43) (2020) 48284–48295.
[33] F. Bertoli, D. Garry, M.P. Monopoli, A. Salvati, K.A. Dawson, The intracellular destiny of the protein corona: a study on its cellular internalization and evolution, ACS Nano 10 (11) (2016) 10471–10479.
[34] C.C. Fleischer, C.K. Payne, Nanoparticle–cell interactions: molecular structure of the protein corona and cellular outcomes, Accounts Chem. Res. 47 (8) (2014) 2651–2659.
[35] T. Gangadhar, S. Nandi, R. Salgia, The role of chemokine receptor CXCR4 in lung cancer, Cancer Biol. Ther. 9 (6) (2010) 409–416.
[36] Y.-N. Zhang, W. Poon, A.J. Tavares, I.D. McGilvray, W.C. Chan, Nanoparticle–liver interactions: cellular uptake and hepatobiliary elimination, J Control Release 240 (2016) 332–348.

[37] D.J. Klionsky, A.J. Meijer, P. Codogno, T.P. Neufeld, R.C. Scott, Autophagy and p70S6 kinase, Autophagy 1 (1) (2005) 59–61.
[38] Z.Y. Yin, G. Gong, C. Zhu, B. Wang, C. Sun, X.H. Liu, et al., Angiopoietin-1 protects neurons by inhibiting autophagy after neuronal oxygen-glucose deprivation/recovery injury, Neuroreport 31 (11) (2020) 825–832.
[39] D. Ren, Q. Zhu, J. Li, T. Ha, X. Wang, Y. Li, Overexpression of angiopoietin-1 reduces doxorubicin-induced apoptosis in cardiomyocytes, J Biomed Res 26 (6) (2012) 432–438.